



## Cu<sub>2</sub>In<sub>2</sub>ZnS<sub>5</sub>/Gd<sub>2</sub>O<sub>2</sub>S:Tb for full solar spectrum photoreduction of Cr(VI) and CO<sub>2</sub> from UV/vis to near-infrared light

Xinjuan Liu<sup>a,\*</sup>, Baibai Liu<sup>a</sup>, Lei Li<sup>b</sup>, Zhihao Zhuge<sup>a</sup>, Pengbin Chen<sup>a</sup>, Can Li<sup>a</sup>, Yinyan Gong<sup>a</sup>, Lengyuan Niu<sup>a</sup>, Junying Liu<sup>c</sup>, Lei Lei<sup>a,\*</sup>, Chang Q. Sun<sup>d</sup>

<sup>a</sup> Institute of Coordination Bond Metrology and Engineering (CBME), College of Materials Science and Engineering, China Jiliang University, Hangzhou, 310018, China

<sup>b</sup> Chongqing Key Laboratory of Extraordinary Coordination Bond and Advanced Materials Techniques (EBEAM), Yangtze Normal University, Chongqing, 408100, China

<sup>c</sup> Research Center for Combustion and Environment Technology, Shanghai Jiao Tong University, Shanghai, 200240, China

<sup>d</sup> School of Electrical and Electronic Engineering, Nanyang Technological University, Singapore, 639798, Singapore



### ARTICLE INFO

#### Keywords:

Full solar spectrum  
Photocatalysis  
Cu<sub>2</sub>In<sub>2</sub>ZnS<sub>5</sub>  
Gd<sub>2</sub>O<sub>2</sub>S  
Co-catalyst  
Reduction

### ABSTRACT

Full solar spectrum active heterogenous photocatalysis for environmental applications remains highly challenging. Here we report the novel Cu<sub>2</sub>In<sub>2</sub>ZnS<sub>5</sub>/Gd<sub>2</sub>O<sub>2</sub>S:Tb (CG) hybrid photocatalysts via a facile solvothermal method for efficient Cr(VI) and CO<sub>2</sub> reduction. The narrow band gap energies of the CG hybrid photocatalysts synthesized via a facile solvothermal method show excellent absorption and catalytic activity in the full solar spectrum. High Cr(VI) reduction rate of 90% and CH<sub>4</sub> production rate of 57.73 μmol h<sup>-1</sup> g<sup>-1</sup> are achieved for CG hybrid photocatalyst with 1 wt.% Gd<sub>2</sub>O<sub>2</sub>S:Tb. The excellent performance is due to the fact that in the hybrid, Gd<sub>2</sub>O<sub>2</sub>S:Tb as cocatalyst, provides more active sites and inhibits the recombination of charge carriers due to the synergistic effect between Cu<sub>2</sub>In<sub>2</sub>ZnS<sub>5</sub> and Gd<sub>2</sub>O<sub>2</sub>S:Tb, consequently improving the photocatalytic reduction activity.

### 1. Introduction

Sunlight as one of the most promising renewable energy resources is an abundant, free, easily available and green resource. Semiconductor photocatalysis utilizing sunlight has attracted significant attention in recent years because of its wide applications in solar energy conversion and environmental purification [1–3]. Especially, artificial photosynthesis via photocatalytic reduction of CO<sub>2</sub> into energy fuels (such as methane, methanol and carbon monoxide etc.), has been regarded as one of the most sustainable and economical strategies to solve the global warming and energy crisis. In this process, broad light absorption range and efficient solar energy conversion are key factors for enhanced photoreduction activity.

To make full use of the solar energy, many approaches have been carried out to extend the light absorption range of wide bandgap semiconductor such as TiO<sub>2</sub> and ZnGe<sub>2</sub>O<sub>4</sub> that respond to visible light, including noble metal depositing, heteroatom doping, dye sensitizing and coupling with other narrow band gap semiconductors [4–6]. Moreover, numerous efforts have been devoted to exploiting novel visible light photocatalysts such as metal oxides, oxynitrides, sulphides, and perovskite for degradation of organic pollutants [7,8], production of hydrogen and oxygen [9], reduction of carbon dioxide and heavy

metal ions [10]. However, the spectral extension reported in the previous works is quite limited, and near infrared (NIR) light that occupies over 50% of the solar energy is scarcely exploited.

The fascinating photoluminescence of up-conversion phosphor and carbon quantum dots (CQDs) offers a strategy to use the NIR light in photocatalytic process. They can act as cocatalyst candidates to harness the NIR light and generate more electron-hole pairs, leading to the enhanced catalytic activity of main photocatalyst. However, their quantum efficiencies are limited due to their extremely narrow absorption band of light at 980 nm and the competition in the light conversion processes. Later, the black hydrogenated TiO<sub>2</sub> was synthesized by introducing disorder in the surface layers of nanophasic TiO<sub>2</sub> to improve the solar light absorption, and it exhibited substantial solar-driven photocatalytic activities in the oxidation of organic molecules and production of hydrogen [11]. Subsequently, NIR light active photocatalysts such as Cu<sub>2</sub>(OH)PO<sub>4</sub> [12], Au-tipped PbSe/CdSe/CdS core/shell/shell heterostructure nanocrystals [13], Ag<sub>2</sub>S [14], Ag<sub>2</sub>O [15], g-C<sub>3</sub>N<sub>4</sub> [16], MoS<sub>2</sub> [17], W<sub>18</sub>O<sub>49</sub> [18], and Black phosphorus [19] have also been reported to show excellent catalytic activity. Noble metal nanoparticles such as Au and Ag with strong surface plasmon resonance effect have been reported to use the NIR light for photocatalysis [20]. Besides, sensitizer such as ZnPc [21], Zn-tri-PcNc [22] and CuPc [23]

\* Corresponding authors.

E-mail addresses: [lxj69635@126.com](mailto:lxj69635@126.com) (X. Liu), [15a0502093@cjlu.edu.cn](mailto:15a0502093@cjlu.edu.cn) (L. Lei).

have also been applied in photocatalysis and photovoltaic conversion for absorbing the NIR light. Nevertheless, the photocatalytic activities of these reported materials are relatively low on account of low photon energy, limited light absorption range and quick recombination of charge carriers [24]. Therefore, the development of cost-effective semiconductor photocatalysts with absorption of full solar light spectrum from UV to NIR light and efficient charge separation is highly desirable, but remains a big challenge.

Recently, transition metal dichalcogenides (TMDs) have aroused particular interest owing to their original structures, outstanding electronic and optical properties as well as their promising applications [25,26]. As typical TMDs, MoS<sub>2</sub> has been regarded as a promising visible light photocatalyst for hydrogen evolution and organic pollutants degradation. In our previous works, many efforts have been devoted to exploiting the transition metal dichalcogenides-based hybrid photocatalysts that are activated by full solar light spectrum. MoSe<sub>2</sub> [27], MoSe<sub>2</sub>/CQDs [28], CuS/graphene [29] and ZnS/graphene [30] composites show excellent catalytic activity under UV, visible and even NIR light irradiation. Currently, multicomponent chalcogenide solid solutions such as Cu-In-Zn-S (CIZS) system have been studied as promising candidates for utilizing solar energy in the fields of photoluminescence, biological imaging and dye-sensitized solar cells due to their tunable band gap properties, chemical stability and low toxicity. Notably, CIZS should also be a promising photocatalyst for effectively utilizing sunlight, but its photocatalytic reduction activity has never been reported, especially in terms of reduction of Cr(VI) and CO<sub>2</sub> under full solar light spectrum irradiation.

Constructing heterostructures photocatalysts can offer the driving forces to improve the electron transfer efficiency and retard the charge recombination, thus resulting in the significantly improved photoactivity. The light converting materials have gained considerable interest in photocatalysis and solar energy collection [31–33]. Though great progress has been made in the coupling of up-conversion phosphor and semiconductor for photocatalysis, little attention has been focused on the catalytic activity of down-converting phosphors-based hybrid photocatalysts, especially in terms of reduction of Cr(VI) and CO<sub>2</sub>. For down-converting phosphors Gd<sub>2</sub>O<sub>2</sub>S:Tb, the emission peak at 546 nm is apparent under 254 nm light excitation [34]. When the Gd<sub>2</sub>O<sub>2</sub>S:Tb is introduced into CIZS, the emission photon energy can excite the CIZS to generate more electron-hole pairs, resulting in the enhanced catalytic activity. Therefore, the coupling of Gd<sub>2</sub>O<sub>2</sub>S:Tb with CIZS to form heterostructure photocatalysts should be an effective way to enhance the catalytic activity in the reduction of Cr(VI) and CO<sub>2</sub> under full solar light spectrum irradiation.

In this work, we report the synthesis of CIZS/Gd<sub>2</sub>O<sub>2</sub>S:Tb (CG) hybrid photocatalysts with full solar (UV-vis-NIR) spectrum responsive for CO<sub>2</sub> and Cr(VI) reduction. To the best of our knowledge, it is the first time to investigate the CG hybrid photocatalysts for CO<sub>2</sub> and Cr(VI) reduction under the radiation of light over the full spectrum. The experimental section is described in Electronic Supplementary Information (ESI†). CG hybrid photocatalysts with 0.5, 1 and 2 wt.% Gd<sub>2</sub>O<sub>2</sub>S:Tb were labelled as CG-0.5, CG-1 and CG-2, respectively. The photo-stability of CG hybrid photocatalysts and possible mechanism were also studied by a series of characterization.

## 2. Result and discussion

### 2.1. Characterizations

Fig. 1 shows the X-ray powder diffraction (XRD) patterns of CIZS and CG-1. All diffraction peaks located at 28.1°, 32.5°, 46.8° and 55.3° in the XRD pattern of CIZS can be well indexed to the (111), (020), (220) and (131) planes of tetragonal phase CIZS (JCPDS 47-1370), respectively [35]. No impurity peak is identified, indicating the good purity of CIZS. For the XRD pattern of CG hybrid photocatalysts, no obvious change can be observed compared with that of CIZS,

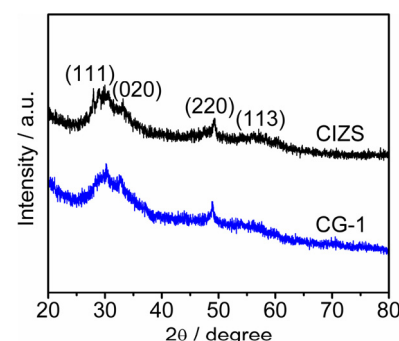


Fig. 1. XRD patterns of CIZS and CG-1.

demonstrating that the coupling of Gd<sub>2</sub>O<sub>2</sub>S:Tb does not result in the development of new crystal orientations or change in preferential orientations of CIZS. Furthermore, there are no diffraction peaks of Gd<sub>2</sub>O<sub>2</sub>S:Tb in the XRD pattern of CG hybrid photocatalysts, which may be owing to the small amount of Gd<sub>2</sub>O<sub>2</sub>S:Tb in the hybrid photocatalysts.

Fig. 2(a) and (b) show the field-emission scanning electron microscopy (FESEM) images of CIZS and Gd<sub>2</sub>O<sub>2</sub>S:Tb. CIZS displays the sheet nanostructure, while Gd<sub>2</sub>O<sub>2</sub>S:Tb nanoplates are aggregated randomly into large sheets during the drying process, as shown in Fig. 2(b). The FESEM image of CG-1 is shown in Fig. 2(c). It can be observed that the Gd<sub>2</sub>O<sub>2</sub>S:Tb is well dispersed into CIZS, indicating the presence of CIZS and Gd<sub>2</sub>O<sub>2</sub>S:Tb in the CG hybrid photocatalysts. In addition, the morphology of CIZS in the CG hybrid photocatalysts is similar to that of CIZS, indicating that the introduction of Gd<sub>2</sub>O<sub>2</sub>S:Tb does not affect the formation of CIZS. The composition of CG-1 was identified by energy dispersive X-ray spectroscopy (EDS) linked to FESEM (Figs. 2(d) and S1). EDS element mapping (elements distribution of Cu, In, Zn, S, Gd, O and Tb) result further confirms the existence of CIZS and Gd<sub>2</sub>O<sub>2</sub>S:Tb in the CG hybrid photocatalysts. No other element peak is observed, indicating the high purity of the products.

Fig. 3(a) and (b) show the low- and high-magnification transmission electron microscopy (HRTEM) images of CG-1. It further confirms the presence of Gd<sub>2</sub>O<sub>2</sub>S:Tb bulk contacting with CIZS sheets. As shown in Fig. 3(b), the fringe spacing of 0.32 nm is observed, which matches well to (111) lattice plane of CIZS [35]. Alongside the CIZS sheet, the lattice spacing of 0.331 nm corresponds to the (100) diffraction plane of Gd<sub>2</sub>O<sub>2</sub>S:Tb [36]. The result strongly demonstrates the formation of CG hybrid photocatalysts. The selected area electron diffraction (SAED) pattern in Fig. 3(c) shows clear diffraction rings and can be well indexed as CIZS and Gd<sub>2</sub>O<sub>2</sub>S:Tb phase, indicating the high crystallinity of CG hybrid photocatalysts.

Fig. 4(a) and (b) show the Fourier transform infrared spectroscopy (FTIR) and Raman spectra of CIZS, CG-0.5, CG-1 and CG-2. The absorption peaks at 3000–3700 and 1000–1450 cm<sup>−1</sup> for all the samples correspond to the surface absorbed water molecules and hydroxyl groups [37]. The absorption band below 500 cm<sup>−1</sup> for all the samples corresponds to the Zn–O and (Zn, Cu)–O stretching modes [38]. A characteristic peak in the Raman spectrum of pure CIZS locates at 295 cm<sup>−1</sup>, corresponding to the feature of A<sub>1</sub> phonon mode of CIZS [39]. For CG hybrid photocatalysts, the main FTIR and Raman spectra are similar to those of pure CIZS, and no new peak corresponding to Gd<sub>2</sub>O<sub>2</sub>S:Tb appears in the FTIR and Raman spectra of CG hybrid photocatalysts, probably due to its low amount and relatively low diffraction intensity.

The composition and chemical state of CG hybrid photocatalysts were characterized by X-ray photoelectron spectroscopy (XPS). Fig. 5 displays the high-resolution spectra of Cu 2p, In 3d, Zn 2p, S 2p, Gd 4d and O 1s peaks of CG-1. For Cu 2p, two peaks at 951.7 and 931.9 eV can be ascribed to Cu 2p<sub>1/2</sub> and Cu 2p<sub>3/2</sub>, respectively [39]. In Fig. 5(b), In 3d has two peaks at 452.4 and 444.9 eV for In 3d<sub>3/2</sub> and In 3d<sub>5/2</sub>,

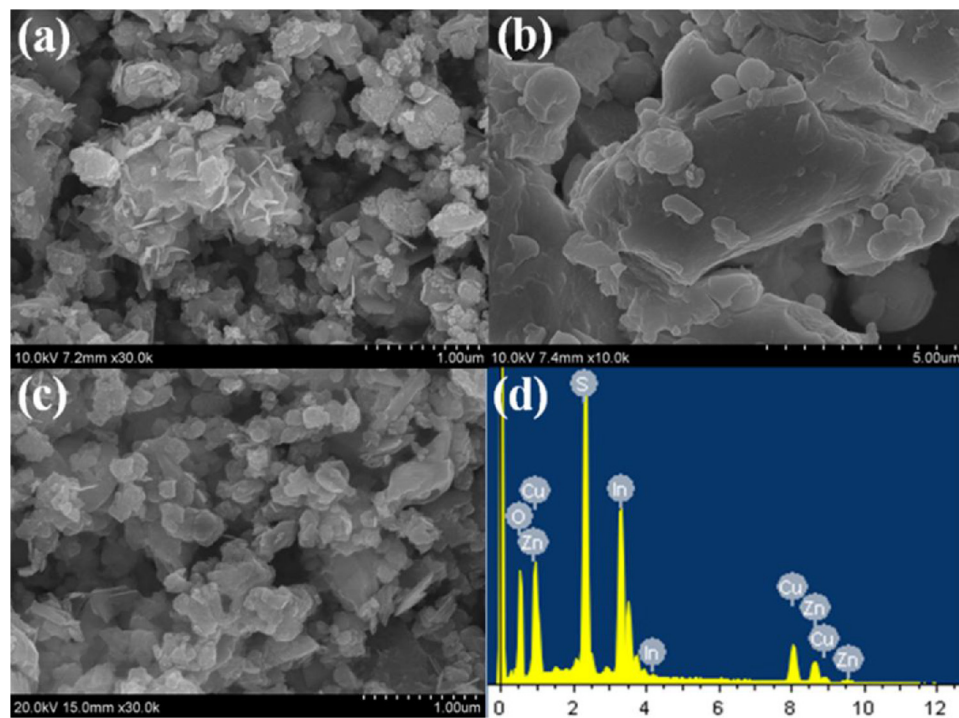


Fig. 2. FESEM images of (a) CIZS, (b)  $\text{Gd}_2\text{O}_2\text{S:Tb}$ , and (c) CG-1; (d) EDS spectrum of CG-1.

respectively, corresponding to the  $\text{In}^{3+}$  state with peak splitting of 7.5 eV [35]. Zn 2p in Fig. 5(c) displays binding energies of 1045.3 (Zn 2p<sub>1/2</sub>) and 1022.1 eV (Zn 2p<sub>3/2</sub>) with a peak split of 23.2 eV, which can be assigned to the  $\text{Zn}^{2+}$  state [40]. The presence of  $\text{S}^{2-}$  is confirmed by the S 2p<sub>1/2</sub> and S 2p<sub>3/2</sub> peaks at binding energies of 162.6 and 161.4 eV, respectively (Fig. 5(d)) [40]. The high-resolution XPS spectra of Gd 4d (Fig. 5(e)) for CG-1 exhibit a peak at 140 eV, corresponding to the Gd [41]. In Fig. 5(f), the peak of O1s at 531.1 eV corresponds to  $\text{Gd}_2\text{O}_3\text{-O}$ , and a higher binding energy of 532 eV is assigned to mixed contributions from  $\text{Gd}_2\text{O}_2\text{S-O}$  [42]. All of the results confirm that the products are composed of CIZS and  $\text{Gd}_2\text{O}_2\text{S:Tb}$ .

The UV-vis-NIR diffuse absorption spectra of CIZS, CG-0.5, CG-1 and CG-2 are shown in Fig. 6(a). It can be observed that CIZS and CG hybrid photocatalysts exhibit obvious absorption in the solar region of 250–2500 nm, especially for the NIR light of 760–2500 nm. Therefore, CIZS and CG hybrid photocatalysts should be regarded as a promising full spectrum (UV, visible and NIR) response photocatalysts. Subsequently, the band gaps of CIZS and CG hybrid photocatalysts are obtained by transformation based on the Kubelka-Munk function versus the energy of light. The band gaps can be estimated to be 0.90, 0.92,

0.94 and 0.97 eV for CIZS, CG-0.5, CG-1 and CG-2, respectively (Fig. 6(b)).

## 2.2. Photocurrent response and electrochemical impedance spectra

The charge transfer and recombination behaviors of photocatalysts are very crucial factors in photocatalytic process, which can be proved by the photocurrent responses and electrochemical impedance spectra (EIS) spectra. Fig. 7(a) shows the transient photocurrent responses of CIZS, CG-0.5, CG-1 and CG-2 under visible light irradiation. It can be clearly seen that the photocurrent quickly decreases to zero when the light is switched off, indicating the recombination of photo-generated charge carriers. The transient photocurrent responses of all samples are reversible and relatively stable at light-on and light-off. The photocurrent of CG hybrid photocatalysts is enhanced compared with that of pure CIZS, which implies that the photo-generated charge carriers are efficiently separated. CG-1 exhibits the highest photocurrent, demonstrating more efficient charge transfer process and longer lifetime of photo-generated charge carriers. Fig. 7(b) shows the typical Nyquist plots of CIZS, CG-0.5, CG-1 and CG-2. The semicircle in the EIS spectra

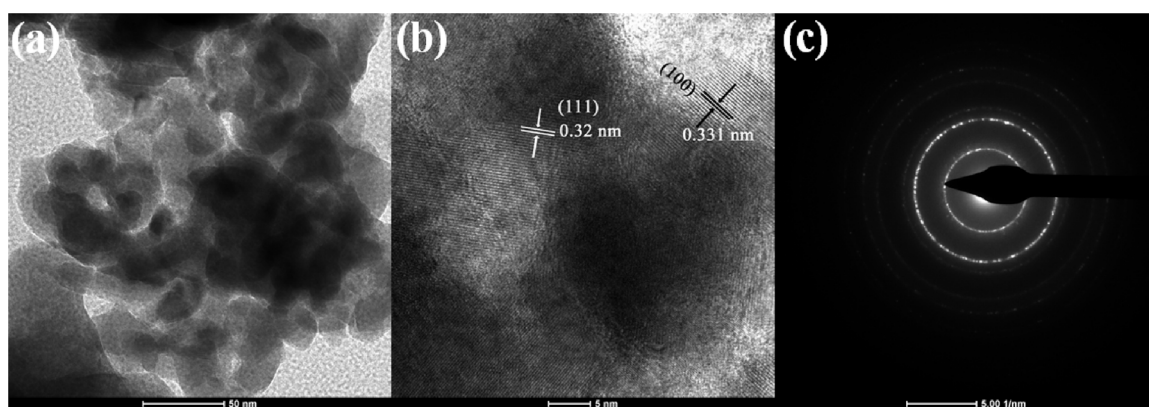


Fig. 3. (a) Low- and (b) high-magnification HRTEM images of CG-1; (c) SAED pattern of CG-1.

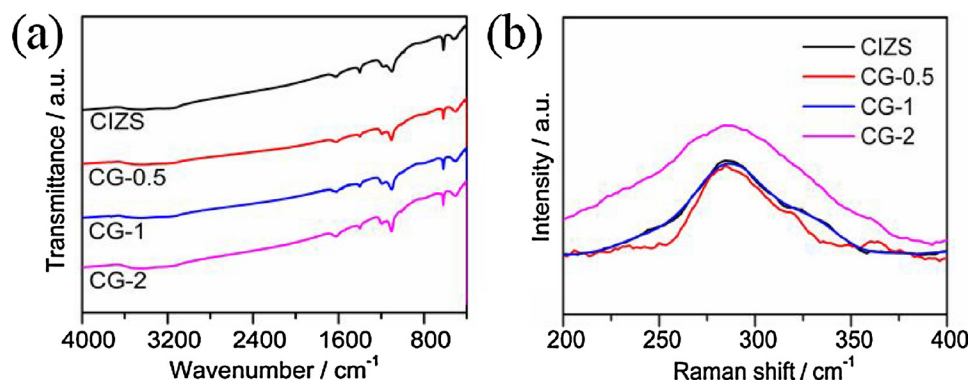


Fig. 4. (a) FTIR and (b) Raman spectra of CIZS, CG-0.5, CG-1 and CG-2.

is ascribed to the contribution from the charge transfer resistance ( $R_{ct}$ ) and constant phase element (CPE) at the photocatalyst/electrolyte interface. The inclined line, resulting from the Warburg impedance  $Z_W$ , corresponds to the ion-diffusion process in the electrolyte. The corresponding equivalent circuit is shown in the inset of Fig. 7(b). The fitted  $R_s$ ,  $R_{ct}$  and CPE for all CG samples are listed in Table S1. It is found that the  $R_{ct}$  values of CG hybrid photocatalysts are smaller than that of pure CIZS, indicating that the recombination of photo-generated charge carriers is more effectively inhibited by introducing the  $\text{Gd}_2\text{O}_2\text{S}:Tb$ . With the increase of  $\text{Gd}_2\text{O}_2\text{S}:Tb$  content, the  $R_s$  decreases and then increases, in accordance with the result of photocurrent responses. The increased  $R_s$  may be due to the fact that the excessive  $\text{Gd}_2\text{O}_2\text{S}:Tb$  can act as recombination center to increase the charge recombination, which is unfavorable for the catalytic process. Fig. S2(a) and (b) show the photoluminescence (PL) and time resolved PL (TRPL) spectra of CIZS, CG-0.5, CG-1 and CG-2. It is found in Fig. S2(a) that the PL intensity decreases with the increase of  $\text{Gd}_2\text{O}_2\text{S}:Tb$  content, confirming that the charge recombination in CG hybrid photocatalysts can be effectively inhibited. The decay curves in Fig. S2(b) are fitted by exponentials to obtain the decay time. The average lifetimes of charge carriers are calculated to be 0.138, 0.174, 0.189 and 0.187 ns for CIZS, CG-0.5, CG-1 and CG-2, respectively. CG-1 shows the longest lifetime, which can improve the charge separation and transfer efficiency, and thus

enhance the photocurrent [43]. The photocurrent responses, EIS, PL and TRPL results demonstrate that CG-1 has the highest separation efficiency of photo-generated charge carriers, in agreement with the result of photocatalytic experiment. The results also demonstrate that the  $\text{Gd}_2\text{O}_2\text{S}:Tb$  content can affect the behaviors of separation and recombination of charge carries in the CG hybrid photocatalysts.

### 2.3. Photocatalytic activity

In order to examine the photocatalytic activity of CIZS and CG hybrid photocatalysts, photocatalytic reduction of Cr(VI) and  $\text{CO}_2$  were studied under UV, visible and NIR light irradiation. Fig. S3 shows the time-resolved absorption spectra of Cr(VI) with CG-1 under NIR light irradiation. It can be found that the absorption of Cr(VI) weakens with the increase of irradiation time, indicating that the Cr(VI) concentration decreases under NIR light irradiation. Furthermore, the Cr(VI) concentration with CG-1 under visible light irradiation was also analyzed using the diphenylcarbazide (DPC) method at 540 nm, as shown in Fig. S4(a). It can be observed that the absorption peaks of Cr(VI) decrease with the increase of irradiation time, demonstrating that the Cr(VI) concentration decreases in the visible light photocatalytic process.

Fig. 8 shows the time-dependent reduction rates of Cr(VI) by CIZS, CG-0.5, CG-1 and CG-2 under UV, visible and NIR light irradiation. It

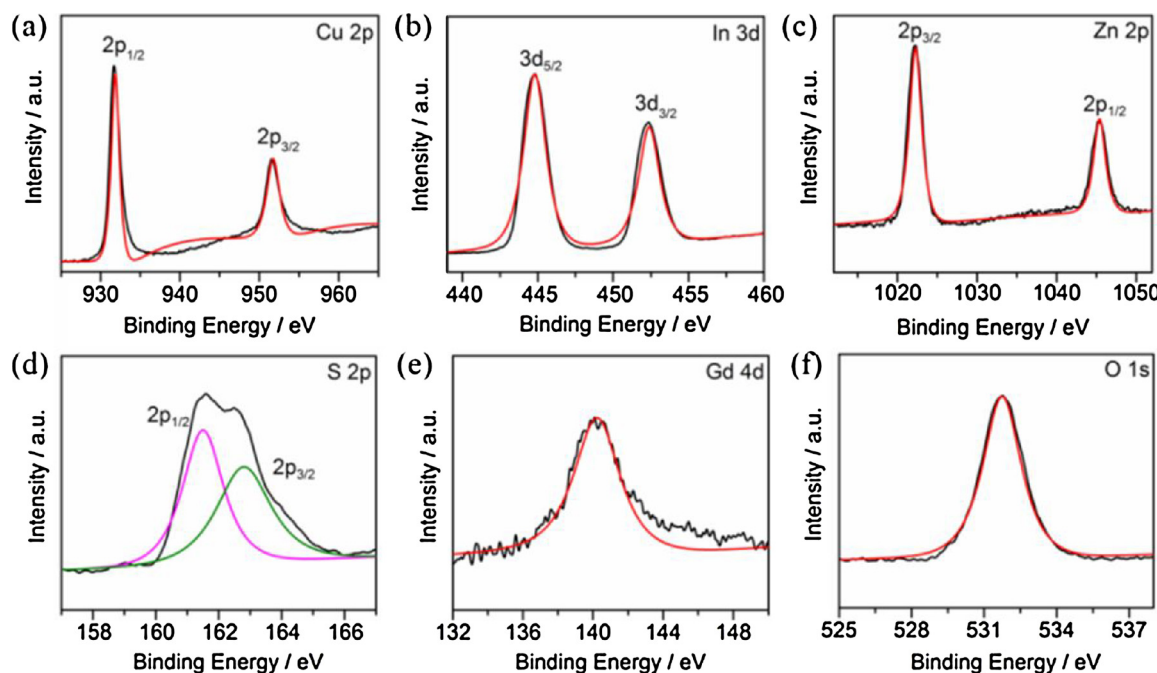


Fig. 5. High-resolution XPS spectra of (a) Cu 2p, (b) In 3d, (c) Zn 2p, (d) S 2p, (e) Gd 4d and (f) O 1s for CG-1.

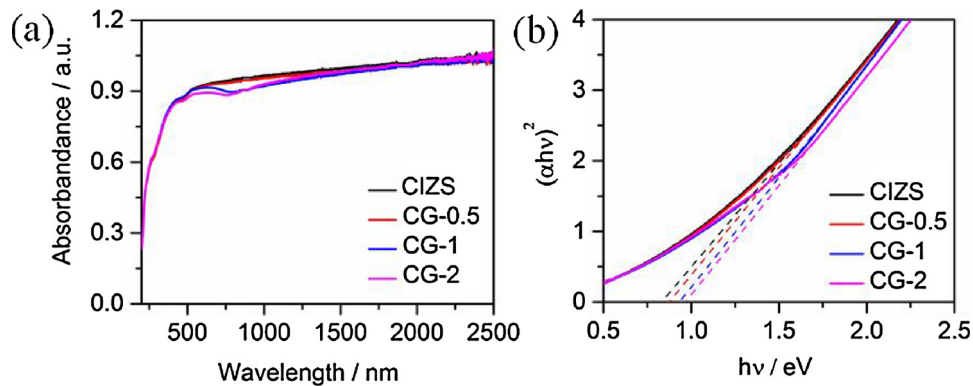


Fig. 6. (a) UV-vis-NIR diffuse absorption spectra and (b) plots of transformed Kubelka-Munk function versus the energy of light.

can be found in Fig. 8(a) that the Cr(VI) concentration has barely changes without the photocatalyst under NIR light irradiation. In all the experiments, the Cr(VI) solution was firstly homogenized for 30 min in darkness, in order to reach the system equilibrium. The normalized temporal concentration changes ( $C/C_0$ ) of Cr(VI) during the photocatalytic process is proportional to the normalized maximum absorbance ( $A/A_0$ ), which can be derived from the change in the Cr(VI) absorption profile during the photocatalysis process.  $C_0$  is the Cr(VI) concentration upon reaching the adsorption equilibrium in the dark for 30 min. Therefore, the adsorption of Cr(VI) is negligible in the photocatalytic reaction process under the studied conditions. The Cr(VI) reduction rate for CIZS is low (77%) owing to the fast recombination of charge carries. However, the catalytic activity is enhanced by the introduction of  $\text{Gd}_2\text{O}_2\text{S}$  in the CIZS to form CG hybrid photocatalysts and depends on the  $\text{Gd}_2\text{O}_2\text{S}$  content. With the increase of  $\text{Gd}_2\text{O}_2\text{S}$  content, the Cr(VI) reduction rate increases. The Cr(VI) reduction rates are 87%, 92% and 87% for CG-0.5, CG-1 and CG-2 after 180 min NIR light irradiation, respectively. As shown in Fig. 8(b), the Cr(VI) reduction rates are 63%, 71%, 93% and 87% for CIZS, CG-0.5, CG-1 and CG-2 after 210 min visible light irradiation, respectively. Under UV light irradiation, the reduction rates are 80%, 85%, 91% and 82% for CIZS, CG-0.5, CG-1 and CG-2 after 60 min irradiation, respectively (Fig. 8(c)). The reduction rates of Cr(VI) obtained by DPC method are 54%, 65%, 73% and 65% for CIZS, CG-0.5, CG-1 and CG-2 under visible light irradiation for 210 min, respectively (Fig. S4(b)). Therefore, CG hybrid photocatalysts exhibit excellent catalytic activity in the reduction of Cr(VI) not only under NIR light irradiation but also under visible and UV light irradiation. The  $\text{Gd}_2\text{O}_2\text{S}$  content can affect the catalytic activity of CG hybrid photocatalysts under the radiation of light over the full spectrum. During photocatalysis, the adsorption ability of the photocatalysts is one of the crucial factors [32,44]. Fig. S5(a) shows the adsorption ability of CG hybrid photocatalysts under the dark condition even in the presence of photocatalyst (CG-1). It can be observed that the time period reaching the adsorption equilibrium is 30 min, and the Cr

(VI) adsorption rate is 34%. The Cr(VI) removal ability by photocatalysis and adsorption using CIZS, CG-0.5, CG-1 and CG-2 was shown in Fig. S5(b-d) under UV, visible and NIR light irradiation, respectively. It can be observed that the maximum Cr(VI) remove rates by photocatalysis and adsorption reach to 93%, 97% and 95% under UV, visible and NIR light irradiation, respectively.

Fig. S6 shows the reaction kinetics in the photocatalytic reduction of Cr(VI) for CIZS and CG hybrid photocatalysts under the radiation of light over the full spectrum. The values of rate constants ( $k$ ) can be obtained by plotting the relationship between  $\ln(C/C_0)$  and irradiation time. The  $k$  is very low and negligible without the photocatalyst under UV, visible and NIR light irradiation. Under NIR and visible light irradiation, the  $k$  follows the order: CG-1 > CG-2 > CG-0.5 > CIZS. Moreover, the  $k$  follows the order under UV light irradiation: CG-1 > CG-0.5 > CG-2 > CIZS. The result shows that CG-1 exhibits the best catalytic activity under NIR even the UV and visible light irradiation, and an appropriate  $\text{Gd}_2\text{O}_2\text{S}$  content is important to the catalytic activity of CG hybrid photocatalysts.

The photo-stability of photocatalysts is very important in practical application. Here, we selected CG-1 as a typical sample to investigate the photo-stability of CG hybrid photocatalysts in the reduction of Cr (VI) with three times of cycling uses, as shown in Fig. 8(d). It is noteworthy that only insignificant decrease in catalytic activity is found after three cycles, which may be due to the loss of photocatalyst during collection process, suggesting the good stability and durability of CG hybrid photocatalysts. Figs. S7 and S8 show the XRD pattern and SEM image of CG-1 after photocatalytic reaction. It can be observed that the crystal structure and morphology of CG-1 do not change before and after the photocatalytic reaction. The composition and chemical state of CG-1 after catalytic reaction were also characterized by XPS (Fig. S9). It can be observed that the composition and chemical state of CG-1 remain unchanged before and after the catalytic reaction, revealing that the CG hybrid photocatalysts are sufficiently stable in the catalytic process. All of the results clearly confirm the good photo-stability of CG

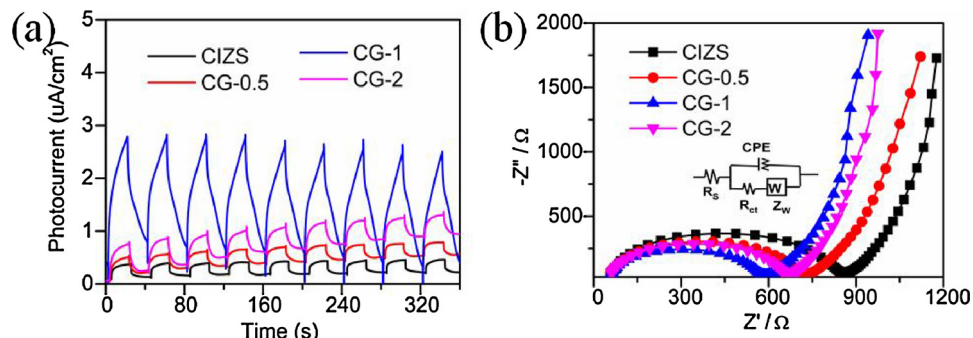
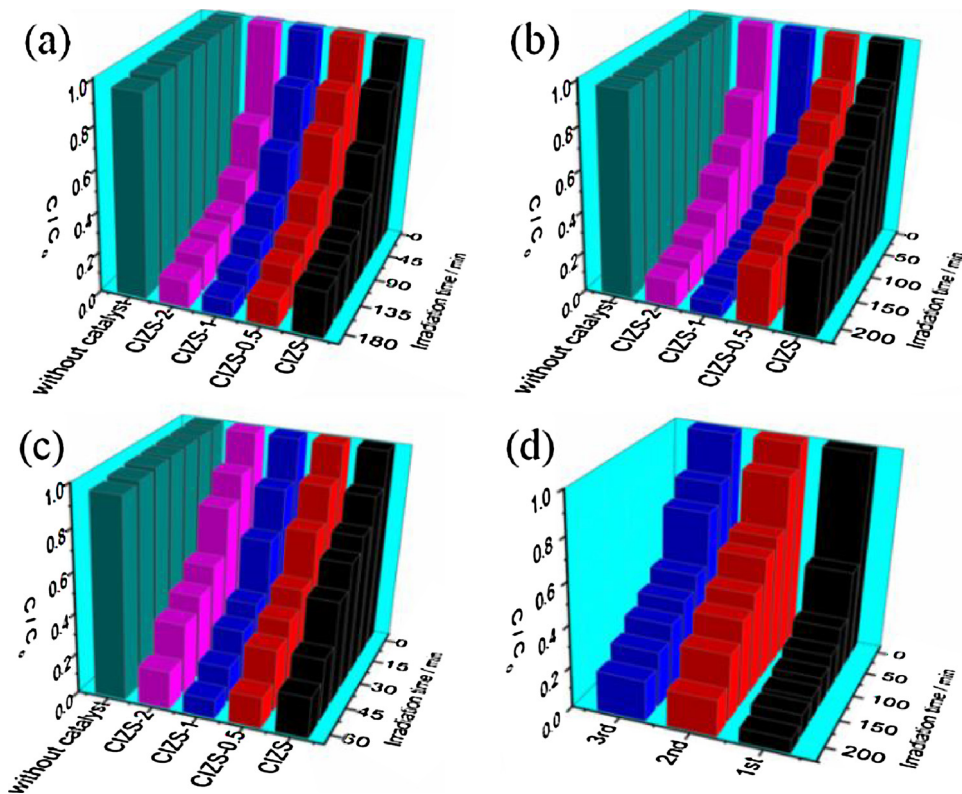


Fig. 7. (a) Transient photocurrent responses and (b) Nyquist plots of CIZS, CG-0.5, CG-1 and CG-2 under visible light irradiation. Inset of b is the corresponding equivalent circuit model.



**Fig. 8.** Photocatalytic reduction of Cr(VI) by CIZS, CG-0.5, CG-1 and CG-2 under (a) NIR, (b) visible and (c) UV light irradiation; (d) photo-stability of CG-1 by investigating its visible light photocatalytic activity with three times of cycling uses.

hybrid photocatalysts under the studied conditions.

Photocatalytic reduction of  $\text{CO}_2$  over CIZS and CG hybrid photocatalysts was performed under Xe lamp irradiation, as shown in Fig. 9.  $\text{CH}_4$  and  $\text{H}_2$  are found in the presence of  $\text{CO}_2$  and catalysts due to the unique electrical band structures. Other products such as CO, methanol and formic acid have also been confirmed experimentally. It is found that no other products such as CO, methanol and formic acid are

produced. The product yield is calculated after 4 h irradiation. As seen in Fig. 9(a) and (b), the  $\text{CH}_4$  and  $\text{H}_2$  yields increase linearly with the increase of irradiation time, indicating that these photocatalysts show excellent photo-stability [45]. CG hybrid photocatalysts afford enhanced photocatalytic reduction of  $\text{CO}_2$  compared with CIZS, attributed mainly to the unique electrical band structures and efficient charge transfer between CIZS and  $\text{Gd}_2\text{O}_2\text{S}: \text{Tb}$ . The catalytic reduction of  $\text{CO}_2$

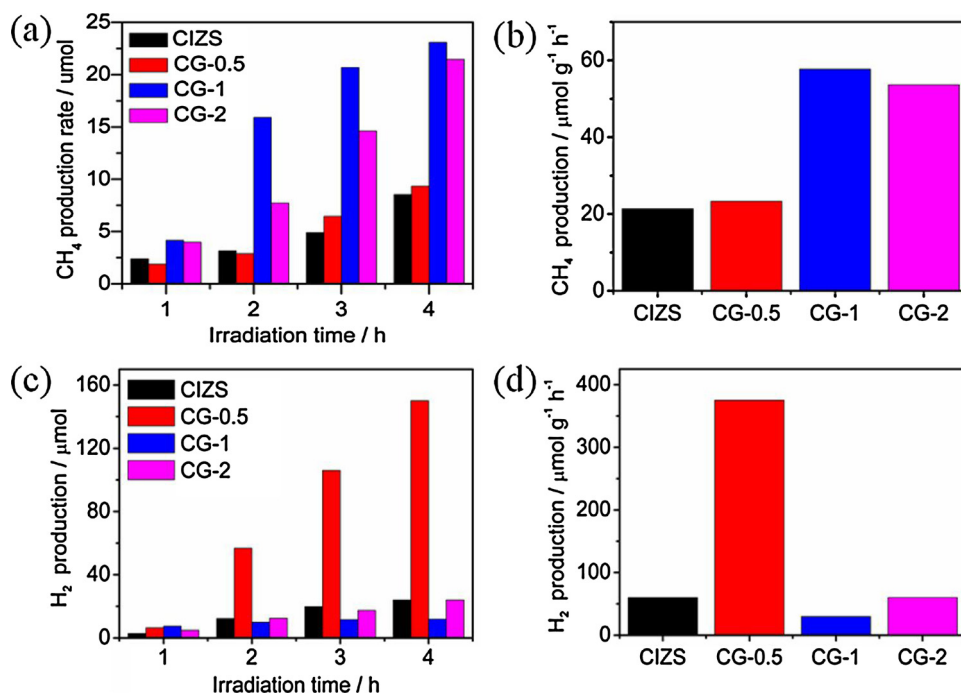


**Fig. 9.** Time-dependent (a)  $\text{CH}_4$  and (c)  $\text{H}_2$  yields and average (b)  $\text{CH}_4$  and (d)  $\text{H}_2$  production rates by CIZS, CG-0.5, CG-1 and CG-2 under Xe lamp irradiation.

over CG hybrid photocatalysts is relevant to the  $\text{Gd}_2\text{O}_2\text{S}$  content. Fig. 9(b) shows the average  $\text{CH}_4$  and  $\text{H}_2$  production rates of CIZS, CG-0.5, CG-1 and CG-2. The  $\text{CH}_4$  and  $\text{H}_2$  production rates are calculated in terms of  $\mu\text{mol h}^{-1}\text{g}^{-1}$ . CIZS exhibits a relatively low  $\text{CH}_4$  and  $\text{H}_2$  production rates with 21.35 and  $60.05\ \mu\text{mol h}^{-1}\text{g}^{-1}$  due to the rapid recombination of photo-induced charge carries. For CG hybrid photocatalysts, the  $\text{CH}_4$  and  $\text{H}_2$  production rates increase firstly and then decrease with the increase of  $\text{Gd}_2\text{O}_2\text{S:Tb}$  content. The average  $\text{CH}_4$  production rates are 23.35, 57.73 and  $53.62\ \mu\text{mol h}^{-1}\text{g}^{-1}$  for CG-0.5, CG-1 and CG-2, respectively. The optimal ratio is 1%. The average  $\text{H}_2$  production rates are 375.25, 29.73 and  $60.13\ \mu\text{mol h}^{-1}\text{g}^{-1}$  for CG-0.5, CG-1 and CG-2, respectively. CG-1 hybrid photocatalyst shows the best ability for the photocatalytic reduction of  $\text{CO}_2$  into  $\text{CH}_4$  due to the transfer of electron from CIZS and  $\text{Gd}_2\text{O}_2\text{S:Tb}$ .

#### 2.4. Possible photocatalytic mechanism

The photocatalytic reaction involves four basic processes as follows: light absorption, charge separation and transport toward the catalyst surface, reactant adsorption and activation, and surface redox reaction pathways and kinetics, which can affect the catalytic activity and products. In catalytic process using CIZS and CG hybrid photocatalysts, the valence band (VB) electrons of photocatalysts can be excited to generate the electron-hole pairs by absorbing the photon energy under light irradiation. Then, the electrons and holes migrate to the catalyst surface to participate in redox reactions and may recombine in transfer process.

The reaction product depends on the band edge positions of semiconductor. The conduction band (CB) and VB can be calculated according to the concept of electronegativity using the following equations:

$$E_{\text{VB}} = X - E^{\text{e}} + 0.5E_{\text{g}} \quad (1)$$

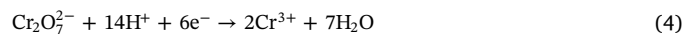
$$E_{\text{CB}} = E_{\text{VB}} - E_{\text{g}} \quad (2)$$

where  $E_{\text{VB}}$  and  $E_{\text{CB}}$  are the VB and CB edge potential.  $X$  is the electronegativity of the semiconductor.  $E_{\text{g}}$  is the band gap of the semiconductor.  $E^{\text{e}}$  is the energy of the free electrons on the hydrogen scale, approximately 4.5 eV. Based on the above equations, the values of  $E_{\text{VB}}$  are calculated to be 0.66, 0.67, 0.68 and 0.69 V for CIZS, CG-0.5, CG-1 and CG-2, respectively. The values of  $E_{\text{CB}}$  are  $-0.24$ ,  $-0.25$ ,  $-0.26$  and  $-0.28$  V for CIZS, CG-0.5, CG-1 and CG-2, respectively. The energy level structures of CIZS and CG hybrid photocatalysts are provided in Scheme 1.

The  $\text{Cr(VI)}/\text{Cr(III)}$  potential (0.51 V vs. NHE, pH = 6.8 [46]) is more positive than the CB of CIZS and CG hybrid photocatalysts. Therefore, the  $\text{Cr(VI)}$  can be reduced to  $\text{Cr(III)}$  by the photo-generated electrons in

catalytic reduction of  $\text{Cr(VI)}$  process. Fig. S10 shows the high resolution XPS spectrum of  $\text{Cr 2p}$  for CG-1 after catalytic reaction. Two peaks at 576.8 eV and 586.8 eV correspond to  $\text{Cr 2p}_{1/2}$  and  $\text{Cr 2p}_{3/2}$  orbitals, which are attributed to the  $\text{Cr(VI)}$  and  $\text{Cr(III)}$ . The result indicates the presence of  $\text{Cr(III)}$  in the catalytic reaction process. Djellabi et al. [47] found that the produced  $\text{Cr(III)}$  existed both-on photocatalyst surface and in the solution. The  $\text{Cr(III)}$  in the solution could be easily removed by precipitation, while the extraction of deposited  $\text{Cr(III)}$  from photocatalyst surface needed to use extraction agents such as citric acid and ethylenediaminetetraacetic acid (EDTA). The  $\text{Cr(III)}$  removal from photocatalyst ( $\text{TiO}_2$ ) surface by the sequential extraction after three washing were 90.13% and 42.62% using citric acid and EDTA, respectively [47].

The role of photo-generated electrons in  $\text{Cr(VI)}$  reduction process is determined by trapping experiment with addition of electron scavenger (Fig. S11) and spin trapping electron paramagnetic resonance (EPR) technique (Fig. S12). As shown in Fig. S11, the addition of electron scavenger decreases largely the catalytic activity, demonstrating that the photo-generated electrons govern the  $\text{Cr(VI)}$  reduction, which is consistent with the literatures [27]. The distinct EPR signals of TEMPO are observed in the dark from Fig. S12. However, the intensity of EPR signals reduces under visible light irradiation, demonstrating that the TEMPO is reduced to TEMPOH by photo-induced electrons [48]. EPR spectra obtained from sample containing TEMPO and CG-1 further proves the presence of photo-induced electrons in the  $\text{Cr(VI)}$  reduction process. The major reaction steps are summarized as follows:

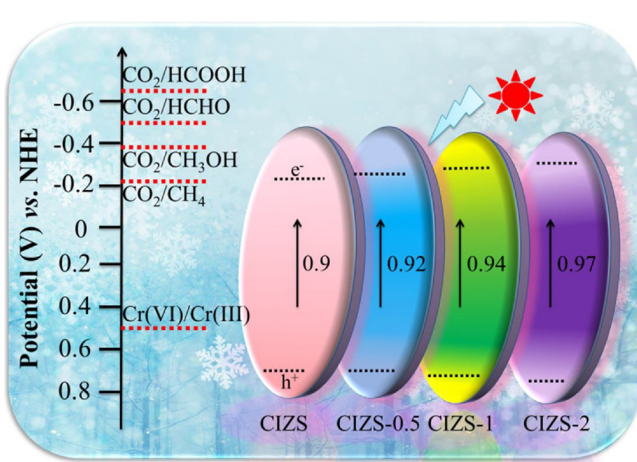


Marinho et al. [49] reported that the hole can produce the hydroxyl radicals from water oxidation, which may re-oxidize  $\text{Cr(III)}$  to  $\text{Cr(VI)}$  and inhibit the reduction rate in the photocatalytic reduction of  $\text{Cr(VI)}$ . Because the VB of CIZS and CG hybrid photocatalysts is negative than the  $\cdot\text{OH}/\text{H}_2\text{O}$  potential (2.27 V, vs. NHE), the holes cannot oxidize  $\text{H}_2\text{O}$  to form  $\cdot\text{OH}$ . Therefore, the  $\text{Cr(VI)}$  can be efficiently reduced in the absence of hole scavenger molecules due to the less oxidizing species. Photocatalytic reduction of  $\text{Cr(VI)}$  over CG hybrid photocatalysts (CG-1) was performed in presence of hole scavenger (oxalic acid (OA)) under visible light irradiation, as shown in Fig. S13. It can be found that the  $\text{Cr(VI)}$  can be completely reduced within less than 30 min, which indicates that the  $\text{Cr(VI)}$  reduction rate can be obviously improved in the presence of hole scavenger. This may be because that the addition of OA can suppress the charge recombination. Similar result was also be observed in the literature [49]. Moreover, because the CB level of CIZS and CG hybrid photocatalysts is positive than the  $\cdot\text{O}_2^-/\text{O}_2$  potential ( $-0.28$  V, vs. NHE), the photo-generated electrons cannot reduce the adsorbed  $\text{O}_2$  to produce  $\cdot\text{O}_2^-$ . Therefore, CIZS and CG hybrid photocatalysts have a weak oxidation ability to degrade the organic pollutants. The photocatalytic degradation of methylene blue (MB) and methyl orange (MO) over CG hybrid photocatalysts (CG-1) was also performed under visible light irradiation to check the oxidation ability. It is found that the MB and MO degradation rates are negligible within 210 min.

In the  $\text{CO}_2$  photoreduction process, the final products are determined by the number and rates of electrons transferred between photo-generated carriers as well as the specific reaction pathway. The CB of CIZS and CG hybrid photocatalysts is more negative than that of the  $\text{CO}_2/\text{CH}_4$  ( $-0.24$  V vs. NHE) [50] and  $\text{H}_2/\text{H}_2\text{O}$  (0 V vs. NHE). Therefore, the electrons can easily reduce  $\text{CO}_2$  to  $\text{CH}_4$  and  $\text{H}_2$ , and the product of  $\text{CO}_2$  photoreduction is  $\text{CH}_4$  and  $\text{H}_2$ . The major reaction steps are summarized as follows:



CG hybrid photocatalysts exhibit the enhanced catalytic activity



Scheme 1. Proposed photocatalytic mechanism for CG hybrid photocatalysts.

compared with pure CIZS due to their synergistic effect. Photocurrent responses, EIS and time resolved PL results demonstrate that the introduction of  $\text{Gd}_2\text{O}_2\text{S:Tb}$  can facilitate the separation and transport and suppress the recombination of photo-generated charge carries, thus lengthening the lifetime of charge carries, in agreement with the result of catalytic experiment. Furthermore, the emission peak for  $\text{Gd}_2\text{O}_2\text{S:Tb}$  locates at 546 nm under 254 nm light excitation, which matches the absorption range of CG hybrid photocatalysts. Therefore, when the  $\text{Gd}_2\text{O}_2\text{S:Tb}$  is introduced into CIZS, the emission photon energy can excite the CG hybrid photocatalysts to generate more electron-hole pairs, resulting in the enhanced catalytic activity. In addition, the specific surface area of photocatalyst is also crucial factor in the catalytic process. Fig. S14 shows the  $\text{N}_2$  adsorption-desorption isotherms of CIZS, CG-0.5, CG-1 and CG-2. According to the Brunauer-Deming-Deming-Teller classification, all CIZS and CG hybrid photocatalysts displays a type IV isotherm with a  $\text{H}_3$  typical hysteresis loop, indicating the presence of mesoporous structure. The specific surface areas are 12.18, 17.36, 20.38 and  $17.72 \text{ m}^2 \text{ g}^{-1}$  for CIZS, CG-0.5, CG-1 and CG-2, respectively. The specific surface area of CG hybrid photocatalysts first increases and then decreases with the increase of  $\text{Gd}_2\text{O}_2\text{S:Tb}$  contents. The relatively higher specific surface area of CG-1 can provide more surface active site, which can facilitate the adsorption of contaminant and photocatalytic process. However, the decreased specific surface area of CG-2 due to the blocking of pores by the stacked  $\text{Gd}_2\text{O}_2\text{S:Tb}$  is not beneficial to its catalytic activity [51]. Based on the above results, the mechanism for the enhanced catalytic activity of CG hybrid photocatalysts arises from the more active sites, the reduced recombination of charge carries, and the light down-converting effect of  $\text{Gd}_2\text{O}_2\text{S:Tb}$ .

### 3. Conclusions

In summary, CG hybrid photocatalysts were successfully synthesized via a facile solvothermal method for Cr(VI) and  $\text{CO}_2$  reduction. The results show that the catalytic activity of CG hybrid photocatalysts is superior to that of pure CIZS due to the synergistic effect of  $\text{Gd}_2\text{O}_2\text{S:Tb}$  and CIZS. High Cr(VI) reduction rate of more than 90% and  $\text{CH}_4$  production rate of  $57.73 \mu\text{mol h}^{-1} \text{ g}^{-1}$  are achieved for the hybrid photocatalyst with 1 wt.%  $\text{Gd}_2\text{O}_2\text{S:Tb}$  under full UV-vis-NIR light irradiation. The excellent photocatalytic activity is ascribed to the good absorption in whole light spectrum, the more active sites, the efficient charge separation, and the light down-converting effect of  $\text{Gd}_2\text{O}_2\text{S:Tb}$ . Moreover, the photo-induced electrons dominate the Cr(VI) and  $\text{CO}_2$  reduction process. The study provides a valuable guiding line on the development of novel photocatalysts that is capable to harness the UV-vis-NIR light.

### Acknowledgements

Financial support from the Province Natural Science Foundation of Zhejiang (No. LY18E060005, LY18E020007 and LQ18E030005), National Natural Science Foundation of China (No. 21401180) are gratefully acknowledged.

### Appendix A. Supplementary data

Supplementary material related to this article can be found, in the online version, at doi:<https://doi.org/10.1016/j.apcatb.2019.02.061>.

### References

- [1] L.Z. Zhang, C. Yang, Z.L. Xie, X.C. Wang, Cobalt manganese spinel as an effective cocatalyst for photocatalytic water oxidation, *Appl. Catal. B: Environ.* 224 (2018) 886–894.
- [2] J.J. Song, Z.F. Huang, L. Pan, K. Li, X.W. Zhang, L. Wang, J.J. Zou, Review on selective hydrogenation of nitroarene by catalytic, photocatalytic and electro-catalytic reactions, *Appl. Catal. B: Environ.* 227 (2018) 386–408.
- [3] M. Wen, K. Mori, Y. Kuwahara, T.C. An, H. Yamashita, Design and architecture of metal organic frameworks for visible light enhanced hydrogen production, *Appl. Catal. B: Environ.* 218 (2017) 555–569.
- [4] Y.Q. Yang, L.C. Yin, Y. Gong, P. Niu, J.Q. Wang, L. Gu, X.Q. Chen, G. Liu, L.Z. Wang, H.M. Cheng, An unusual strong visible-light absorption band in red anatase  $\text{TiO}_2$  photocatalyst induced by atomic hydrogen-occupied oxygen vacancies, *Adv. Mater.* 30 (2018) 1704479.
- [5] Y. Jiang, H.Y. Ning, C.G. Tian, B.J. Jiang, Q. Li, H.J. Yan, X.L. Zhang, J.Q. Wang, L.Q. Jing, H.G. Fu, Single-crystal  $\text{TiO}_2$  nanorods assembly for efficient and stable cocatalyst-free photocatalytic hydrogen evolution, *Appl. Catal. B: Environ.* 229 (2018) 1–7.
- [6] X.J. Liu, L.K. Pan, T. Lv, Z. Sun, C.Q. Sun, Sol-gel synthesis of  $\text{Au}/\text{N-TiO}_2$  composite for photocatalytic reduction of Cr (VI), *RSC Adv.* 2 (2012) 3823–3827.
- [7] Z. Wei, J.S. Hu, K.J. Zhu, W.Q. Wei, X.G. Ma, Y.F. Zhu, Self-assembled polymer phenylethynylcopper nanowires for photoelectrochemical and photocatalytic performance under visible light, *Appl. Catal. B: Environ.* 226 (2018) 616–623.
- [8] H.B. Yin, Y. Kuwahara, K. Mori, H.F. Cheng, M.C. Wen, Y.N. Huo, H. Yamashita, Localized surface plasmon resonances in plasmonic molybdenum tungsten oxide hybrid for visible-light-enhanced catalytic reaction, *J. Phys. Chem. C* 121 (2017) 23531–23540.
- [9] D.L. Zhong, W.W. Liu, P.F. Tan, A.Q. Zhu, Y. Liu, X. Xiong, J. Pan, Insights into the synergy effect of anisotropic {001} and {230} facets of  $\text{BaTiO}_3$  nanocubes sensitized with CdSe quantum dots for photocatalytic water reduction, *Appl. Catal. B: Environ.* 227 (2018) 1–12.
- [10] Q.J. Xiang, B. Cheng, J.G. Yu, Graphene-based photocatalysts for solar-fuel generation, *Angew. Chem. Int. Ed.* 54 (2015) 11350–11366.
- [11] X.B. Chen, L. Liu, Y.Y. Peter, S.S. Mao, Increasing solar absorption for photocatalysis with black hydrogenated titanium dioxide nanocrystals, *Science* 331 (2011) 746–750.
- [12] G. Wang, B.B. Huang, X.C. Ma, Z.Y. Wang, X.Y. Qin, X.Y. Zhang, Y. Dai, M.H. Whangbo,  $\text{Cu}_2(\text{OH})\text{PO}_4$ , a near-infrared-activated photocatalyst, *Angew. Chem. Int. Ed.* 52 (2013) 4810–4813.
- [13] C. Pak, Y.W. Ju, K. Lee, W.D. Kim, Y. Yoo, D.C. Lee, Extending the limit of low-energy photocatalysis: dye reduction with  $\text{PbSe/CdSe/CdS}$  core/shell/shell nanocrystals of varying morphologies under infrared irradiation, *J. Phys. Chem. C* 116 (2014) 25407–25414.
- [14] W. Jiang, Z.M. Wu, X.N. Yue, S.J. Yuan, H.F. Lu, B. Liang, Photocatalytic performance of  $\text{Ag}_2\text{S}$  under irradiation with visible and near-infrared light and its mechanism of degradation, *RSC Adv.* 5 (2015) 24064–24071.
- [15] W. Jiang, X.Y. Wang, Z.M. Wu, X.N. Yue, S.J. Yuan, H.F. Lu, B. Liang, Silver oxide as superb and stable photocatalyst under visible and near-infrared light irradiation and its photocatalytic mechanism, *Ind. Eng. Chem. Res.* 54 (2015) 832–841.
- [16] Y.R. Li, Z.W. Wang, T. Xia, H.X. Ju, K. Zhang, R. Long, Q. Xu, C.M. Wang, L. Song, J.F. Zhu, J. Jiang, Y.J. Xiong, Implementing metal-to-ligand charge transfer in organic semiconductor for improved visible-near-infrared photocatalysis, *Adv. Mater.* 28 (2016) 6959–6965.
- [17] L.H. Zhi, H.L. Zhang, Z.Y. Yang, W.S. Liu, B.D. Wang, Interface coassembly of mesoporous  $\text{MoS}_2$  based-frameworks for enhanced near-infrared light driven photocatalysis, *Chem. Commun.* 52 (2016) 6431–6434.
- [18] G. Xi, S. Ouyang, P. Li, J. Ye, Q. Ma, N. Su, H. Bai, C. Wang, Ultrathin  $\text{W}_{18}\text{O}_{49}$  nanowires with diameters below 1 nm: synthesis, near-infrared absorption, photoluminescence, and photochemical reduction of carbon dioxide, *Angew. Chem. Int. Ed.* 51 (2012) 2395–2399.
- [19] M.S. Zhu, Y. Osakada, S. Kim, M. Fujitsuka, T. Majima, Black phosphorus: a promising two dimensional visible and near-infrared-activated photocatalyst for hydrogen evolution, *Appl. Catal. B: Environ.* 217 (2017) 285–292.
- [20] W.Y. Jiang, S. Bai, L.M. Wang, X.J. Wang, L. Yang, Y.R. Li, D. Liu, X.N. Wang, Z.Q. Li, J. Jiang, Y.J. Xiong, Integration of multiple plasmonic and co-catalyst nanostructures on  $\text{TiO}_2$  nanosheets for visible-near-infrared photocatalytic hydrogen evolution, *Small* 12 (2016) 1640–1648.
- [21] X.H. Zhang, L.J. Yu, C.S. Zhuang, T.Y. Peng, R.J. Li, X.G. Li, Highly asymmetric phthalocyanine as a sensitizer of graphitic carbon nitride for extremely efficient photocatalytic  $\text{H}_2$  production under near-infrared light, *ACS Catal.* 4 (2014) 162–170.
- [22] X.H. Zhang, T.Y. Peng, L.J. Yu, R.J. Li, Q.Q. Li, Z. Li, Visible/near-infrared-light-induced  $\text{H}_2$  production over  $\text{g-C}_3\text{N}_4$  co-sensitized by organic dye and zinc phthalocyanine derivative, *ACS Catal.* 5 (2015) 504–510.
- [23] Z.J. Zhang, W.Z. Wang, D. Jiang, J.Y. Xu, CuPc sensitized  $\text{Bi}_2\text{MoO}_6$  with remarkable photo-response and enhanced photocatalytic activity, *Catal. Commun.* 55 (2014) 15–18.
- [24] Y.H. Sang, H. Liu, A. Umar, Photocatalysis from UV/vis to near-infrared light: towards full solar-light spectrum activity, *ChemCatChem* 7 (2014) 559–573.
- [25] B.B. Liu, X.J. Liu, J.Y. Liu, C.J. Feng, Z. Li, C. Li, Y.Y. Gong, L.K. Pan, S.Q. Xu, C.Q. Sun, Efficient charge separation between  $\text{UiO-66}$  and  $\text{ZnIn}_2\text{S}_4$  flowerlike 3D microspheres for photoelectrochemical properties, *Appl. Catal. B: Environ.* 226 (2018) 234–241.
- [26] X.J. Liu, L.K. Pan, T. Lv, G. Zhu, Z. Sun, C.Q. Sun, Microwave-assisted synthesis of CdS-reduced graphene oxide composites for photocatalytic reduction of Cr(VI), *Chem. Commun.* 47 (2011) 11984–11986.
- [27] H.P. Chu, X.J. Liu, B.B. Liu, G. Zhu, W.Y. Lei, H.G. Du, J.Y. Liu, J.W. Li, C. Li, C.Q. Sun, Hexagonal 2H-MoSe<sub>2</sub> broad spectrum active photocatalyst for Cr(VI) reduction, *Sci. Rep.* 6 (2016) 35304.
- [28] Z. Ren, X. Liu, H. Chu, H. Yu, Y. Xu, W. Zheng, W. Lei, P. Chen, J. Li, C. Li, Carbon quantum dots decorated MoSe<sub>2</sub> photocatalyst for Cr(VI) reduction in the UV-vis-NIR photon energy range, *J. Colloid Interface Sci.* 488 (2017) 190–195.
- [29] J. Wu, B.B. Liu, Z.X. Ren, M.Y. Ni, C. Li, Y.Y. Gong, W. Qin, Y.L. Huang, C.Q. Sun, X.J. Liu, CuS/RGO hybrid photocatalyst for full solar spectrum photoreduction from

- UV/vis to near-infrared light, *J. Colloid Interface Sci.* 517 (2017) 80–85.
- [30] Z.X. Ren, L. Li, B.B. Liu, X.J. Liu, Z. Li, X. Lei, C. Li, Y.Y. Gong, L.Y. Niu, L.K. Pan, Cr (VI) reduction in presence of ZnS/RGO photocatalyst under full solar spectrum radiation from UV/vis to near-infrared light, *Catal. Today* 315 (2018) 46–51.
- [31] X.J. Liu, L.K. Pan, J.L. Li, K. Yu, Z. Sun, C.Q. Sun, Light down-converting characteristics of ZnO-Y<sub>2</sub>O<sub>3</sub>:Eu<sup>3+</sup> for visible light photocatalysis, *J. Colloid Interface Sci.* 404 (2013) 150–154.
- [32] X.J. Liu, X.J. Wang, H.L. Li, J.L. Li, L.K. Pan, J. Zhang, G.Q. Min, Z. Sun, C.Q. Sun, Enhanced visible light photocatalytic activity of ZnO doped with downconversion NaSrBO<sub>3</sub>:Tb<sup>3+</sup> phosphors, *Dalton Trans.* 44 (2015) 97–103.
- [33] X.J. Liu, X.J. Wang, H.L. Li, L.K. Pan, T. Lv, Z. Sun, C.Q. Sun, Microwave-assisted synthesis of ZnO-Y<sub>3</sub>Al<sub>5</sub>O<sub>12</sub>:Ce<sup>3+</sup> composites with enhanced visible light photocatalysis, *J. Mater. Chem.* 22 (2012) 16293–16298.
- [34] L. Lei, S.J. Zhang, H. Xia, Y. Tian, J.J. Zhang, S.Q. Xu, Controlled synthesis of lanthanide-doped Gd<sub>2</sub>O<sub>3</sub>S nanocrystals with novel excitation-dependent multicolor emissions, *Nanoscale* 9 (2017) 5718–5724.
- [35] T.T. Hong, Z.F. Liu, J. Zhang, G.M. Li, J.Q. Liu, X.Q. Zhang, S.H. Lin, Flower-like Cu<sub>2</sub>In<sub>2</sub>ZnS<sub>5</sub> nanosheets: a novel promising photoelectrode for water splitting, *ChemCatChem* 8 (2016) 1288–1292.
- [36] Y. Song, H. You, Y. Huang, M. Yang, Y. Zheng, L. Zhang, N. Guo, Highly uniform and monodisperse Gd<sub>2</sub>O<sub>3</sub>:Ln<sup>3+</sup> (Ln = Eu, Tb) submicrospheres: solvothermal synthesis and luminescence properties, *Inorg. Chem.* 49 (2010) 11499–11504.
- [37] S. Marta, A.B. Fuertes, Chemical and structural properties of carbonaceous products obtained by hydrothermal carbonization of saccharides, *Chem. Eur. J.* 15 (2009) 4195–4203.
- [38] S. Muthukumaran, M. Ashok kumar, Structural, FTIR and photoluminescence properties of ZnS:Cu thin films by chemical bath deposition method, *Mater. Lett.* 93 (2013) 223–225.
- [39] Y.F. Liu, F.Q. Huang, Y. Xie, H.L. Cui, W. Zhao, C.Y. Yang, N. Dai, Controllable synthesis of Cu<sub>2</sub>In<sub>2</sub>ZnS<sub>5</sub> nano/microcrystals and hierarchical films and applications in dye-sensitized solar cells, *J. Phys. Chem. C* 117 (2013) 10296–10301.
- [40] T. Huang, Y.T. Luo, W. Chen, J.C. Yao, X.H. Liu, Self-assembled MoS<sub>2</sub>-GO framework as an efficient cocatalyst of CuInZnS for visible-light driven hydrogen evolution, *ACS Sustain. Chem. Eng.* 6 (2018) 4671–4679.
- [41] J. Thirumalai, R. Chandramohan, S. Valanarasu, T.A. Vijayan, R.M. Somasundaram, T. Mahalingam, S.R. Srikumar, Shape-selective synthesis and opto-electronic properties of Eu<sup>3+</sup>-doped gadolinium oxysulfide nanostructures, *J. Mater. Sci.* 44 (2009) 3889–3899.
- [42] J.J. Dolo, H.C. Swart, J.J. Terblans, E. Coetsee, O.M. Ntwaeborwa, B.F. Dejene, X-ray photoelectron spectroscopy analysis for undegraded and degraded Gd<sub>2</sub>O<sub>3</sub>:Tb<sup>3+</sup> phosphor thin films, *Phys. B: Condens. Matter* 407 (2012) 1586–1590.
- [43] L.T. Ma, H.Q. Fan, J. Wang, Y.W. Zhao, H.L. Tian, G.Z. Dong, Water-assisted ions in situ intercalation for porous polymeric graphitic carbon nitride nanosheets with superior photocatalytic hydrogen evolution performance, *Appl. Catal. B: Environ.* 190 (2016) 93–102.
- [44] X.J. Liu, H.P. Chu, J.L. Li, L.Y. Niu, C. Li, H.L. Li, L.K. Pan, C.Q. Sun, Light converting phosphor-based photocatalytic composites, *Catal. Sci. Technol.* 5 (2015) 4727–4740.
- [45] S. Ma, J. Xie, J.Q. Wen, K.L. He, X. Li, W. Liu, X.C. Zhang, Constructing 2D layered hybrid CdS nanosheets/MoS<sub>2</sub> heterojunctions for enhanced visible-light photocatalytic H<sub>2</sub> generation, *Appl. Surf. Sci.* 391 (2017) 580–591.
- [46] F.F. Jing, R.W. Liang, J.H. Xiong, R. Chen, S.Y. Zhang, Y.H. Li, L. Wu, MIL-68(Fe) as an efficient visible-light-driven photocatalyst for the treatment of a simulated waste-water contain Cr(VI) and malachite green, *Appl. Catal. B: Environ.* 206 (2017) 9–15.
- [47] R. Djellabi, F.M. Ghorab, S. Nouacer, A. Smara, O. Khireddine, Cr(VI) photocatalytic reduction under sunlight followed by Cr(III) extraction from TiO<sub>2</sub> surface, *Mater. Lett.* 176 (2016) 106–109.
- [48] W.W. He, H.M. Jia, J.H. Cai, X.N. Han, Z. Zheng, W.G. Wamer, J.J. Yin, Production of reactive oxygen species and electrons from photoexcited ZnO and ZnS nanoparticles: a comparative study for unraveling their distinct photocatalytic activities, *J. Phys. Chem. C* 120 (2016) 3187–3195.
- [49] B.A. Marinho, R.O. Cristóvão, R. Djellabi, J.M. Loureiro, R.A.R. Boaventura, V.J.P. Vilar, Photocatalytic reduction of Cr(VI) over TiO<sub>2</sub>-coated cellulose acetate monolithic structures using solar light, *Appl. Catal. B: Environ.* 203 (2017) 18–30.
- [50] L. Yuan, Y.J. Xu, Photocatalytic conversion of CO<sub>2</sub> into value-added and renewable fuels, *Appl. Surf. Sci.* 342 (2015) 154–167.
- [51] W. Qin, T.Q. Chen, L.K. Pan, L.Y. Niu, B.W. Hu, D.S. Li, J.L. Li, Z. Sun, MoS<sub>2</sub>-reduced graphene oxide composites via microwave assisted synthesis for sodium ion battery anode with improved capacity and cycling performance, *Electrochim. Acta* 153 (2015) 55–61.